Science
AAAS

Supplementary Materials for

Intergenerational inequities in exposure to climate extremes

Wim Thiery *et al.*

Corresponding author: Wim Thiery, wim.thiery@vub.be

DOI: 10.1126/science.abi7339

The PDF file includes:

Supplementary Materials for Age-dependent extreme event exposure

Wim Thiery[1,2], Stefan Lange[3], Joeri Rogelj[4,5], Carl-Friedrich Schleussner[6,7], Lukas Gudmundsson[2], Sonia I. Seneviratne[2], Marina Andrijevic[6,7], Katja Frieler[3], Kerry Emanuel[8], Tobias Geiger[3,9], David N. Bresch[10,11], Fang Zhao[12,3], Sven N. Willner[3], Matthias Büchner[3], Jan Volkholz[3], Nico Bauer[3], Jinfeng Chang[13,14], Philippe Ciais[14,15], Marie Dury[16], Louis François[16], Manolis Grillakis[17], Simon N. Gosling[18], Naota Hanasaki[19], Thomas Hickler[20,21], Veronika Huber[22], Akihiko Ito[19], Jonas Jägermeyr[23,24,3], Nikolay Khabarov[5], Aristeidis Koutroulis[25], Wenfeng Liu[14,26], Wolfgang Lutz[27,5], Matthias Mengel[3], Christoph Müller[3,28], Sebastian Ostberg[3], Christopher P. O. Reyer[3], Tobias Stacke[29], and Yoshihide Wada[5]

[1]Vrije Universiteit Brussel, Department of Hydrology and Hydraulic Engineering, Brussels, Belgium
[2]ETH Zurich, Institute for Atmospheric and Climate Science, Zurich, Switzerland
[3]Potsdam Institute for Climate Impact Research (PIK), Member of the Leibniz Association, Potsdam, Germany
[4]Imperial College London, Grantham Institute for Climate Change and the Environment, London, UK
[5]International Institute for Applied Systems Analysis (IIASA), Laxenburg, Austria
[6]Climate Analytics, Berlin, Germany
[7]Humboldt University, Integrative Research Institute on Transformations of Human-Environment Systems, Berlin, Germany
[8]Massachusetts Institute of Technology, Lorenz Center, Cambridge, MA, USA
[9]Deutscher Wetterdienst (DWD), Climate and Environment Consultancy, Stahnsdorf, Germany
[10]ETH Zurich, Institute for Environmental Decisions, Zurich, Switzerland
[11]Federal Office of Meteorology and Climatology MeteoSwiss, Zurich, Switzerland
[12]East China Normal University, School of Geographic Sciences, Shanghai, China
[13]Zhejiang University, College of Environmental and Resource Sciences, Hangzhou, China
[14]Institut Pierre Simon Laplace, Laboratoire des Sciences du Climat et de l'Environnement, CEA CNRS UVSQ, Gif sur Yvette, France
[15]The Cyprus Institute, Climate and Atmosphere Research Center (CARE-C), Nicosia, Cyprus
[16]University of Liège, Unit for Modelling of Climate and Biogeochemical Cycles, Liège, Belgium
[17]Foundation for Research and Technology Hellas, Institute for Mediterranean Studies, Rethimno, Greece
[18]University of Nottingham, School of Geography, Nottingham, UK

[19]National Institute for Environmental Studies, Tsukuba, Japan
[20]Goethe University Frankfurt, Institute of Physical Geography, Frankfurt, Germany
[21]Senckenberg Biodiversity and Climate Research Centre (SBiK-F), Frankfurt, Germany
[22]Universidad Pablo de Olavide, Department of Physical, Chemical and Natural Systems, Sevilla, Spain
[23]NASA Goddard Institute for Space Studies, New York, NY, USA
[24]Columbia University, Center for Climate Systems Research, New York, NY, USA
[25]Technical University of Crete, School of Environmental Engineering, Chania, Greece
[26]China Agricultural University, College of Water Resources and Civil Engineering, Beijing, China
[27]University of Vienna, Wittgenstein Centre for Demography and Global Human Capital, Vienna, Austria
[28]Zhejiang University, China Academy for Rural Development, Hangzhou, China
[29]Helmholtz-Zentrum Hereon, Institute of Coastal Research, Geesthacht, Germany

Materials and Methods

The aim of this study is to quantify, in the most robust way possible, the global- and regional-scale increase in exposure to climate extremes for younger generations. To this end, we integrate the exposure of an average member of a birth cohort to extreme events across their lifetime and subsequently compare these results across cohorts and regions. This is achieved by combining five sources of data, which are explained hereafter.

Employed data First, we developed the largest multi-model biophysical impact projections database available to date as part of the Inter-Sectoral Impact Model Intercomparison Project phase 2b (ISIMIP2b) (*16*). Following the ISIMIP2b protocol, we performed simulations with 15 impact models that represent variables relevant for the six extreme event categories described below (CARAIB (*17*), LPJ-GUESS (*18*), LPJmL (*19, 20*), ORCHIDEE (*21*), VISIT (*22, 23*), GEPIC (*24*), PEPIC (*25, 26*), CLM4.5 (*27, 28*), H08 (*29*), JULES-W1 (*30*), MPI-HM (*31, 32*), PCR-GLOBWB (*33,34*), WaterGAP2 (*35,36*), HWMId-humidex (*37*), and KE-TG (*38*)). These process-based models represent the state of the art of global-scale hydrological, vegetation, agricultural, land surface, heat stress, and tropical cyclone modeling (*39–45*). Each model pro-

vides relevent biophysical impact variables such as runoff, crop yields, or soil moisture at a spatial resolution of $0.5^\circ \times 0.5^\circ$ and at daily to annual time scales. The impact models are each driven by up to four downscaled and bias-adjusted (*46*) global climate models (GCMs; GFDL-ESM2M (*47*), HadGEM2-ES (*48*), IPSL-CM5A-LR (*49*), and MIROC5 (*50*)) participating in the fifth phase (*51*) of the Coupled Model Intercomparison Project (CMIP5) under pre-industrial, historical, and RCP 2.6, 6.0 and 8.5 climate forcings. GCMs are designed to capture the spatially-explicit climate response to rising greenhouse gas concentrations and other anthropogenic forcings; as such, they are the cornerstone of scientific knowledge on future climate change. Here, the four GCMs were selected based on data availability and representativeness of the entire CMIP5 ensemble (see Supplementary Text 5 for a detailed description of the selection, downscaling, and bias adjustment procedure). Besides transient historical and future climate information, our simulations represent other human influences via input data mimicking historical socioeconomic development until 2005 and assuming fixed year-2005 conditions thereafter. Overall, our extreme event data set consists of 273 global-scale extreme event projections spanning the period 1861–2099 (table S2) and 101 pre-industrial control simulations covering on average 542 years each. A more detailed description of the data is provided in (*37*).

Second, we employ data on life expectancy at the age of 5 available from the United Nations World Population Prospects (*52*), indicating the number of years a 5-year old would be expected to live if mortality patterns prevailing at the time of observation (year to which this period indicator pertains) were to remain constant throughout their lifetimes. The data is available at the country, regional, and global scale (fig. S4) in 5-year blocks for 1950-1955 to 2015-2020. From this data, we calculate cohort life expectancy at birth which adjusts for child mortality 0-4 because child mortality distorts the pattern that shall be studied. First, we translate the data to annual values using linear interpolation, assume the life expectancy value is representative for the middle year of the 5-year block, and linearly extrapolate life expectancy from 2017 to 2025

in every country. To capture the entire length of the life span starting with birth, we subsequently add 5 years and assign the value to the birth year of the respective cohort, thereby assuming that this value represents life expectancy at birth excluding child mortality. Finally, we translate this indicator from period to cohort life expectancy by adding 6 years to the value of the period life expectancy estimate at birth (*53*). This is based on a rather conservative assumption of future increases in life expectancy given the current uncertainty about future mortality trends. We note that that this life expectancy data ignores impacts from climate change. Our approach thus follows UN fertility and mortality projections, but omits climate change feedbacks on population dynamics.

Third, future GMT trajectories are derived from scenarios compiled in support of the IPCC Special Report on Global Warming of 1.5 °C (SR1.5) (*54, 55*) and were subsequently made available through the Integrated Assessment Modeling Consortium and the International Institute for Applied Systems Analysis (*56, 57*). We select three marker scenarios: two scenarios limiting global warming to 1.5 °C and 2.0 °C above pre-industrial levels (*58*), respectively, and a third scenario consistent with current (2020) Nationally Determined Contributions (NDCs) – also referred to as the current pledges scenario (fig. S1). The 1.5 °C and NDC scenarios (originally labelled 'MESSAGEix-GLOBIOM 1.0_LowEnergyDemand' and 'MESSAGE-GLOBIOM 1.0_ADVANCE_INDC', respectively) were developed with the Integrated Assessment Model MESSAGE-GLOBIOM version 1.0 (*59*). The 2.0 °C scenario was derived using IMAGE version 3.0.1 (*60*). The 2 °C compatible scenario is assessed by the IPCC SR1.5 to keep warming below 2 °C with at least 66 % probability, whereas the 1.5 °C scenario limits warming to 1.5 °C with 50 % probability but potentially exceeds this level temporarily by less than 0.1 °C (*54*). The GMT anomalies in 2091–2100 compared to the pre-industrial reference period (1850–1900) are 1.4 °C, 1.7 °C and 2.4 °C for the 1.5 °C, the 2.0 °C and the current pledges scenario, respectively (fig. S1).

Fourth, gridded population reconstructions and projections are obtained from the ISIMIP2b input data repository. Historical reconstructions are based on version 3.2 of the History Database of the Global Environment (HYDE3.2) (*61*) while future projections are derived from a gravity-based downscaling model (*62*) under the Middle-of-the-Road Shared Socioeconomic Pathway 2 (SSP2) (*63*). Social and economic trends of the SSP2 scenario do not markedly shift from the historical trends. Most countries complete the demographic transition, and the population growth levels off in the second half of the century. Under SSP2, all countries in the world are projected to develop with medium fertility, mortality and migration trends (*64*). The gridded future population projections account for population growth, urbanization level, and spatial urbanization pattern by incorporating variations of these patterns across regions and SSPs (*62*). For population change, countries are categorized according to fertility and income into three groups (high fertility, low fertility with high incomes, and low fertility), whereas for urbanization, countries are grouped based on income alone (Low, Medium and High income). While population density evolves over time according to these drivers, climate-induced changes in migration, urbanisation, fertility, and mortality are not considered in this data set, and therefore not in our approach. We analysed the uncertainty associated with the gridded population data by testing the sensitivity of our results to using gridded population projections under an alternative SSP. Using SSP3 – a pathway considered inconsistent with RCP2.6 – instead of SSP2 showed little sensitivity of the results to the SSP choice, reflecting the fact that our analysis builds on within-country relative population density variability rather that on absolute population totals.

Finally, we use country-scale cohort size data provided by the Wittgenstein Centre and available through its Human Capital Data Explorer (*65*). We consider cohort sizes of the year 2020 and linearly interpolate the 5-year block data to annual time scale, assuming the cohort size value to be valid for the center year of the block.

Extreme event definition. A detailed description of the processing of the ISIMIP2b simulations is provided in Ref. (*37*) and summarised hereafter. We consider 6 extreme event categories: wildfires, crop failure, droughts, river floods, heatwaves, and tropical cyclones. We select these six extreme event categories because we know from existing studies (*16, 66*) that these hazards (i) will increase in frequency, intensity, and/or duration with projected climate change, (ii) can lead to strong impacts when they occur, and (iii) can be tackled comprehensively in a modelling framework such as ISIMIP. For each category and simulated calendar year, we compute the land fraction per grid cell exposed at least once to an extreme event as defined in table S1. As such, the land fraction annually exposed to extreme events becomes a comparable quantity across event categories.

Since the 8 considered global hydrological models do not provide flood extent and apply different routing schemes (*67*), we employ the global-scale river routing model CaMa-Flood (*68*) to compute the land area exposed to river flooding using daily gridded runoff from the global hydrological models as input (table S2). For tropical cyclones, we use the average exposure over a 100-member ensemble of tropical cyclone tracks downscaled from GCM output (*38*). While the strongest increases in tropical cyclone impacts are expected from increasing cyclone intensities (*38, 69*), our projections also show a rise in tropical cyclone frequency under continued warming, consistent with (*37, 38*). For wildfires, we quantify the pure climate change effect on burned area using a suite of global vegetation models (see Supplementary Text 6 for more details). A grid cell is considered to be exposed to a heatwave in a given year if the Heat Wave Magnitude Index daily (HWMId) (*70, 71*) of that year exceeds the 99^{th} percentile of the HWMId distribution under pre-industrial climate conditions of that grid cell. For droughts, heatwaves, and crop failure, we define the extreme event occurrence based on the exceedance of a pre-industrial percentile threshold (table S1). While the exact percentile value is an arbitrary choice, the approach allows for a robust estimation of the threshold values thanks to the long

time span of the pre-industrial control simulations. Moreover, a sensitivity analysis with multiple heatwave definitions showed only little sensitivity of the relative exposure changes at the global scale, suggesting a limited influence of the choice of the pre-industrial percentile value on the analysis of the historical and future impact model simulations. Finally, we also analyse lifetime cold spell exposure, which we define as the counterpart of heatwaves (see Supplementary Text 3).

Exposure calculation. In this study, we integrate the exposure of an average person in any country or region to climate hazards across their lifetime. This cohort analysis considers land areas only and is performed across 178 countries (fig. S7), 11 regions (fig. S4) and the globe.

We first compute country-scale spatial averages of annual land area exposure weighted by population totals of the corresponding year over all available historical, RCP 2.6, 6.0 and 8.5 simulations. This way, our exposure assessment accounts for temporal changes in population density under a Middle-of-the-Road scenario. The resulting time series is then mapped onto the SR1.5 scenarios (1.5 °C, 2 °C and NDCs, respectively) by selecting from the concatenated historical-RCP series the year with the GMT anomaly closest to the annual anomaly in each SR1.5 scenario, thereby effectively using the ISIMIP2b hazard simulations as damage functions (time-shift approach (*72, 73*); fig. 1 left panel). While the analysis can also be performed directly on the RCPs, we decide to apply the time-shift approach because (i) of the increasing policy relevance of low-end warming scenarios like the 1.5°C and 2°C-compatible scenarios; (ii) the ISIMIP2b framework only samples a small set of greenhouse gas concentration pathways (i.e. three RCPs), whereas we here analyse a range of potential warming scenarios (see below); and (iii) we aim to better align hazard projections arising from climate models with different transient climate response to cumulative carbon emissions (TCRE). Both in ISIMIP2b and the SR1.5 scenarios, GMT anomalies are computed using the 1850-1900 historical period (51-year

average) as reference (*37, 74*). Simulations whereby the absolute GMT difference with the SR1.5 scenario in any year exceeds 0.2 °C are excluded to avoid that low-end RCP projections (e.g. RCP 2.6) inform high-end warming scenarios (e.g. current pledges). Our assumption that the simulated hazards are scenario-independent is generally valid for the considered extreme event categories (*37*) and allows us to maximise the hazard information considered in each SR1.5 scenario. Moreover, a comparison of absolute lifetime exposure (see below) of the 2020 birth cohort under RCP2.6 computed, on the one hand, directly from the RCP2.6 projections, and reconstructed, on the other hand, by applying the time-shift approach to the RCP2.6, 6.0, and 8.5 projections, shows a close correspondence between both approaches (fig. S17). From this we conclude that the time-shift approach is a valid method for translating RCP-based projections to alternative GMT trajectories in the context of our analysis. That said, some aspects of these extreme events show a lagged response to global mean temperature increase, making our assessment conservative (see Supplementary Text 2).

Next, we accumulate for each simulation, country and birth year within the period 1960-2020 the extreme event exposure across an average life span in that country. As life expectancy extends up to the year 2113 in some countries and birth cohorts, we assume that beyond 2099, annually exposed land fractions, GMT anomalies and gridded population densities are constant at the 2090-2099 average. In contrast, for some spatial units and early birth years, the life expectancy at birth may not extend until 2020; for those individuals still alive in 2020 the lifetime exposure accounts for the average, not actual life span. To obtain lifetime exposure values at the regional and global scale, we compute for each birth cohort the weighted spatial average of the country-scale exposure using the size of that particular cohort in each country as weighing factor. Analogous to the well-established distinction between the Eulerian and Lagrangian perspective in atmospheric science and between the period and cohort approach in demography, we suggest that the resulting lifetime extreme event exposure values represent the

Lagrangian/cohort view on climate change hazards.

Computing the multi-model arithmetic mean per extreme event category then enables the comparison of different birth cohorts (fig. 1 middle panel), whereby the results combine the effect of changes in extreme event occurrence as a consequence of climate change and the change in life expectancy in that spatial entity.

Exposure multiplication factor. To analyse the lifetime exposure data, we use the exposure multiplication factor (EMF), which is defined as

$$EMF = \frac{E_{\text{new}}}{E_{\text{ref}}} \tag{1}$$

where E_{ref} is the lifetime exposure of a person born in the reference year 1960 – that is, all people being 60 years old on 31 December 2020 – and E_{new} is the lifetime exposure of a person born in a later year. This metric allows us to compare birth cohorts across a range of birth years (fig. 1 right panel). For instance, an EMF of 2 for a newborn and E_{ref} of 3.5 heatwaves implies that a person born in a given country in 1960 will on average face 3.5 heatwaves across their lifetime, whereas a person born in 2020 on will on average face 7 heatwaves. To avoid EMF values being infinite, we assign the value of 100 in the exceptional cases when extreme events emerge in a country or region. The EMF metric relates to the probability ratio metric used in previous studies (*75–77*), where the probability ratio is generally used as a ratio of frequencies of occurrence with probabilities limited to $[0, 1]$ by definition. However, the EMF metric is a ratio of event counts (not of event probabilities), and explicitly includes exposure next to hazards, thereby moving towards more comprehensive risk definitions (*76*).

We consider three approaches to aggregate the information across extreme event categories. The first method computes the geometric mean across the EMF per event category. In this ap-

proach, percent changes in each of the categories equally contribute to the total change, but the approach yields conservative estimates in spatial units not affected by one or several categories under past and future conditions (e.g., tropical cyclones in high-latitude countries). Uncertainties in this approach are computed as the geometric mean of the per-category EMF computed based on the ensemble's 25^{th} and 75^{th} percentile lifetime exposure relative to the multi-model mean exposure under pre-industrial climate conditions. The second approach is to calculate the geometric mean of the lifetime exposure across the six considered event categories and subsequently compute the EMF. The third approach is to compute the harmonic mean across the EMF per event category. The harmonic mean is suited for computing the mean across ratios (such as the EMF) and is the most conservative of the Pythagorean means. Note that the arithmetic mean or the sum are not considered here because the results would be dominated by the strong increase in heatwave occurrence. The sensitivity to the aggregation procedure is visualised in fig. S3; while the first and third aggregation method yield consistent results, the second approach yields substantially higher exposure estimates. Taking a conservative approach, all further cross-category results are based on the first aggregation method.

Exposure scaling with GMT. To derive the EMFs shown in fig. 2, we first construct 28 stylised GMT trajectories. The trajectories are obtained through piecewise linear interpolation between five scenarios: a present-day constant temperature (taken here as the 2009 GMT anomaly of 0.87 °C), a linear temperature increase from 0.87 °C in 2009 to 3.5 °C by 2100, and the three SR1.5 scenarios (1.5 °C, 2 °C, NDC). The resulting scenarios thereby cover, in 2100, the 0.87 – 3.5 °C GMT anomaly range with a 0.1 °C increment (fig. S1).

For each pathway, we subsequently compute the lifetime exposure per spatial unit and event category following the methodology explained above. As reference for the EMF calculation, we consider the average exposure of a person with year-1960 life expectancy under pre-

industrial climate conditions. To this end, we first compute, for each of the 101 pre-industrial control simulations, the lifetime exposure for 100 bootstrapped time series. We then pool the resulting exposure values for all available simulations within that extreme event category, and calculate the arithmetic mean from the resulting distribution. The pre-industrial control exposure thereby samples from one distribution comprising uncertainty from both internal variability and structural climate and impact model deficiencies.

Once the EMF is calculated per extreme event category, the multi-event EMF is obtained by computing the geometric mean across the EMF values per category (see above). The resulting EMF values are subsequently smoothed using a three-element moving average along the vertical and visualised in fig. 2. Note that in fig. 2, uncertainty increases along the y-axis as fewer hazard projections are available to sample from towards higher warming levels. This sampling artefact explains the apparent reduction in droughts and river floods EMF for some cohorts above 3°C warming relative to pre-industrial (fig. 2).

Next to the EMF, we also analyse the probability of experiencing, under pre-industrial climate conditions, the lifetime exposure values obtained under the stylised pathways. To this end, we calculate the empirical inverse percentiles from the pre-industrial control distribution of the lifetime exposure under each of the stylised GMT trajectories. To obtain the pre-industrial exposure distribution aggregated across the six extreme event categories, we first select 1 000 random combinations of one simulation per extreme event category and subsequently compute in each combination the geometric mean EMF across the categories. Since each random combination consists of 100 lifetime exposure values obtained via bootstrapping (see above), this yields a distribution of 100 000 lifetime exposure values. Like with the EMF fields, the resulting probability fields are smoothed using a three-element moving average along the vertical, except for tropical cyclones, where a fourth-order polynomial is fitted to the threshold probability contour to account for the higher uncertainties in these projections obtained from a

single impact model. The results are visualised as grey contours in fig. 2 and denote the 99.99^{th} percentile, that is, above and right of these contours, one has less than 0.01 % probability of living such life under pre-industrial climate conditions. We refer to the latter case as living an unprecedented life.

With the exception of wildfires and tropical cyclones, our extreme events are defined based on extreme percentiles estimated from the pre-industrial control simulations (table S1) (*37*). Due to a statistical artefact (*78, 79*), the expected relative frequency of exceedance of those percentiles (or of falling below for the 2.5^{th} crop yield and soil moisture percentiles) may potentially be larger in data that was not used to estimate the percentiles (such as data from the historical simulations and the future scenario simulations) than in the pre-industrial control data. However, we believe that this issue can be disregarded in our analysis, because (i) we use a very large sample of pre-industrial control simulations (542 years on average) to estimate the percentile values in each simulation, and (ii) our analysis consists of relative changes between cohort lifespans that all fall entirely outside of the base period.

While fig. 2 is inspired by the burning ember diagrams shown in various IPCC reports (*80–82*), we acknowledge that our results cannot be directly translated into this risk framework, primarily because we only consider 2 dimensions of risk in our assessment, that is, hazard and exposure. Further work could aim at including vulnerability into the assessment, for instance by incorporating vulnerability projections and associated adaptation potentials (*83*) in the analysis.

Life expectancy versus climate change. To isolate the contribution of life expectancy change to the total change in lifetime exposure, we repeat the lifetime exposure calculation but apply it to the pre-industrial control simulations (see details below; figs. S15–S16). Assuming this term corresponds to the pure life expectancy effect in the absence of climate change, the residual represents the contribution from climate change.

Data and code availability

Data Availability All materials that have contributed to the reported results are available from Zenodo at https://zenodo.org/record/5497633, including the postprocessed ISIMIP2b data. Correspondence and requests for further materials should be addressed to W.T. (wim.thiery@vub.be). The raw ISIMIP2b impact simulations and gridded population data are available at https://esg.pik-potsdam.de/search/isimip/, the life expectancy data at https://population.un.org/wpp/Download/Standard/Mortality/, the cohort size data at http://dataexplorer.wittgensteincentre.org/wcde-v2/, and the IPCC SR1.5 Scenario data at https://data.ene.iiasa.ac.at/iamc-1.5c-explorer.

Code Availability All codes used for the analyses are available through the github repository of the Department of Hydrology and Hydraulic Engineering at VUB (https://github.com/VUB-HYDR/2021_Thiery_etal_Science).

Supplementary Text

Supplementary Text 1 – Country-level analysis

Breaking the analysis down to country scale highlights strong spatial disparities (figs. S7–8). Lifetime heatwave exposure for the 2020 birth cohort relative to the 1960 birth cohort increases in every country in the world and under all future scenarios considered (fig. S7a-b). However, in several countries the 2020 birth cohort will face more than 10 times as many extreme heatwaves compared to the 1960 birth cohort under current pledges. This is for instance the case in countries in Central Africa, the Middle East and West and Southeast Asia. Under a 1.5 °C scenario, these multiplication factors are often substantially reduced. Similar patterns emerge for the other extreme event categories (fig. S8), though the multiplication factors are subject to higher uncertainty and in some cases indicate reduced exposure, for instance in exposure to crop failures in several Eurasian countries under 1.5 °C warming. Aggregated across all categories, most countries ultimately show a decrease in the exposure multiplication factor going from the current pledges scenario to 1.5 °C of global warming (fig. S7c-d), highlighting a clear incentive for younger generations of limiting global warming to 1.5 °C instead of the 2.6–3.1 °C expected from current pledges (*84, 85*).

Our drought definition is based on the frequency of occurrence of extremely low monthly soil moisture values during at least seven consecutive months (table S1) as computed by 8 global vegetation models and global hydrological models from the ISIMIP biomes and water sector, respectively (CLM4.5, H08, LPJmL, JULES-W1, MPI-HM, ORCHIDEE, PCR-GLOBWB, and WaterGAP2; table S2). Thus, we mechanistically account for changes in both precipitation and evapotranspiration in our drought projections. If precipitation increases in a region according to a GCM projection, the hazard simulation driven by this GCM might project less droughts. This is, for instance, the case in Russia under 1.5°C warming and current pledges,

and in parts of Scandinavia under 1.5°C warming (fig. S8e-f). But if the evapotranspiration increase is larger than the precipitation increase (especially during the dry season), drought frequency may increase despite projected increases in precipitation, like is the case in East Africa (fig. S8e-f) (*86, 87*). This also explains why one region may face an increase in exposure to both droughts and river floods (e.g. Southern Africa and large parts of Asia; fig. S8e-h).

Supplementary Text 2 – Why our estimates may be considered conservative

Our approach yields conservative lifetime exposure estimates for at least six reasons. First, it treats consecutive extreme events (*88*) affecting a specific location within a calendar year as one, leading to an underestimation of the number of events in present-day as well as their increase in frequency. Second, it only considers changes in the frequency of extreme events, neglecting possible increases in event intensity and duration (*71*). For tropical cyclones, for instance, projected increases in storm intensity can be considered equally important (*38*), whereas heatwave duration and intensity are increasing next to heatwave frequency (*89*). Third, we do not take into account the effects of compounding extremes, even though, for instance, severe droughts, heatwaves and crop failures tend to co-occur (*88, 90–93*). Fourth, we only consider exposure to local hazards, yet extreme events such as crop failures may lead to regional or even global food price instability when occurring in isolation or concurrently (*81, 92, 94*). Fifth, we employ stringent definitions of extreme events, with for instance heatwaves occurring only about four times in a lifetime on average for the 1960 birth cohort (fig. 1 middle panel). Several extreme event categories therefore occur only over part of the globe (*37*), leading to an underrepresented risk when aggregating across extreme event categories. Finally, some aspects of the extreme event categories we consider demonstrate a lagged response to global warming. This notably applies for tropical cyclones, which cause substantial impacts via the storm surge they generate. These storm surges are amplified by background sea level rise (*95*) which lags

the global mean temperature increase by decades to centuries (*96, 97*). This lagged response further augments inter-generational inequity, and this to the extent that even the already committed sea level rise will enhance lifetime exposure of generations well beyond the ones we consider in this study (*96, 97*). On shorter time scales, this reasoning also applies to wildfires, as fuel aridity may build up over several years in response to a long-term warming trend (*98*). Overall, these six reasons highlight that our current results may underestimate changes in actual extreme event exposure and thereby underscore the benefits of climate action for current and future young generations.

Supplementary Text 3 – Cold spells

Next to the six extreme event categories considered in this study, the influence on climate change on cold spell exposure could also be considered. To this end, we consider a grid cell to be exposed to a cold spell in a given year if the Cold Wave Magnitude Index daily (CWMId) of that year exceeds the 99^{th} percentile of the CWMId distribution under pre-industrial climate conditions of that grid cell. We define the CWMId as the maximum magnitude of all cold periods occurring in a year, where a cold period is a period of at least six consecutive days with daily maximum temperature falling below a threshold value T_{pi10} which is defined as the 10^{th} percentile of daily maximum temperatures under pre-industrial climate conditions, centered on a 31-day window. The magnitude of each cold period in a year is the sum of the daily magnitudes on the consecutive days composing the cold period, with daily magnitude calculated according to $M_d(T_d) = 0$ if $T_d \geq T_{\mathrm{pi75}}$ else $(T_{\mathrm{pi75}} - T_d)/(T_{\mathrm{pi75}} - T_{\mathrm{pi25}})$, where T_d is the daily maximum temperature on day d of the cold period and T_{pi25} and T_{pi75} are the 25^{th} and 75^{th} percentile, respectively, of the annual minimum of the daily maximum temperature under pre-industrial climate conditions. To estimate T_{pi10}, T_{pi25}, and T_{pi75}, we use more than 400 years of daily maximum temperature data at $0.5^\circ \times 0.5^\circ$ spatial resolution representing pre-industrial

climate conditions as available from the ISIMIP2b climate input data set. Based on these more than 400 years of temperature data we subsequently derive the 99^{th} percentile of the CWMId distribution under pre-industrial climate conditions. As such, we characterise cold spells as the mirror of heatwave events (except for the period which we require to be six instead of three days).

The results of the analysis indicate an overall reduction of exposure to cold spells under increasing global mean temperature levels and for younger cohorts (fig. S18a). Except for a few countries in West Asia, lifetime cold spell exposure reduces consistently across most countries, with the strongest reductions in Africa, the Middle East, Europe, Canada, and parts of South America (fig. S18b).

Supplementary Text 4 – Vulnerability, impacts and adaptation

Our study is deliberately limited to *exposure* to climate *hazards*, given that both adaptation over time and age-dependent vulnerability are extremely difficult to quantify. In that sense, we compute changes in the hazards that people face throughout their lifetime (e.g. a heatwave or a river flood), but make no call about the *risk* or *impact* which they generate (e.g. mortality, infrastructure damage). By altering their vulnerabilities, communities can also adapt to the changes in exposure to hazards. For the extreme event categories considered here, these adaptation options can take many forms: e.g. changing crop types, agricultural management (irrigation, fertiliser), flood protection, reservoir deployment and management, fire management, and improved warning systems. Depending on the adaptation options that communities will (be able to) choose, the level of risk arising from the hazard exposure will vary.

While adaptive capacities may increase over time, extreme events result in detrimental impacts already today, even in developed countries with very high adaptive capacity (see, for instance, the 2019-2020 wildfires in California and Australia). Moreover, for many develop-

ing countries, increased adaptive capacity is needed to address today's climate risks – it does not imply that these countries can cope with unprecedented future hazards even under very optimistic scenarios of socio-economic development. Recent research showed that adaptive capacities are far from uniformly rising Andrijevic2020a and that it will take until well into the 21st century for many developing countries to reach current OECD levels. Overall, there are huge differences in adaptive capacities between countries with no signs that this gap will drastically reduce in the next decades, and even in countries with high adaptive capacities, it is unsure whether entire populations will be able to adapt to severe climate change impacts. Finally, we note the existence of quite hard (physiological) limits to adaptation for several of the extreme events considered in this study. For instance, a wet-bulb temperature of 35°C defines the limit of human survivability (*99–101*). In other cases, migration may be the final adaptation option, which may in turn change both exposure and vulnerability to (a set of) hazards. For instance, a poor Ugandan farmer migrating to the Capital to escape from increasing crop failure may end up settling in one of Kampala's informal settlements which are very prone to flooding, heat stress, and vector-borne diseases (*102, 103*).

Overall, the aspect of changing vulnerability and adaptive capacity requires careful consideration and the absence of a framework to quantitatively integrate future vulnerabilities into climate risk scenarios is why our analysis focuses explicitly on exposure to climate hazards instead of climate risk.

A cohort-based approach raises the question about its relationship to discounting over time to adequately account and weigh intergenerational interests. However, the concept of discounting does not apply to our study given its focus on extreme event exposure instead of climate change impacts. Discounting is commonly used as a methodological approach within cost-benefit analysis (CBA). Yet, our cohort-based extreme event exposure differs from the CBA frameworks, because it only maps out the consequences and uncertainties of different future

climate change pathways in terms of extreme event exposure. Incorporating an exposure perspective, such as ours, within a CBA would require to value the exposures and aggregate them into a cost or welfare metric, since discounting can only be applied to value and welfare metrics. Such aggregation – including the discounting – implicitly assumes that exposures between different groups are comparable and, therefore, trade-offs can be resolved. In principle, the results of the extreme event exposures can serve as input to such analysis, but it requires to value the exposures and aggregate them.

Next to informing a CBA, the extreme event exposure results could also inform a rights-based approach. Rights-based approaches argue for "a general right against risking" (*104*). Rights-based approaches are related to the precautionary principle and relate future risks implied by current action to the infringement on future opportunities and the exercising of basic rights.

In recent years, climate change and the risks for future generations has been increasingly brought to courts. The cohort-based extreme event exposure approach can help to inform this debate. However, we refrain from suggesting criteria or requirements that should be applied to derive the level of climate change. A comprehensive consideration of competing rights would need to take a broader set of rights into account and could not only rely on extreme event exposure. The priorities of competing rights and the weighing of competing rights requires a broader decision analysis framework that is beyond the scope of the present analysis. Finally, the methodological difference between CBA- and rights-based approaches does not necessarily imply a stronger or weaker level of future climate change and therefore higher or lower near term emissions. This is partly due to the sensitivity of CBA results to the choice of the discount rate (*105*) and the role competing rights can play.

Supplementary Text 5 – GCM selection and bias-adjustment procedure

Global Climate Models (GCMs) allow to simulate climate and weather extremes under historical and future atmospheric conditions. The ISIMIP2b climate forcing builds on a selection of GCM output from the fifth phase of the Coupled Model Intercomparison Project (CMIP5) (*106*). The ISIMIP2b forcing data covers four of the CMIP5 GCMs (IPSL-CM5A-LR, HadGEM2-ES, MIROC5, GFDL-ESM2M). Uncertainty of future greenhouse gas emissions is spanned through scenarios, which are the Representative Concentration Pathways (RCPs) (*107*) used in CMIP5 and consequently in the IPCC's Fifth Assessment Report. In support for the IPCC Special Report on global warming of 1.5 °C, ISIMIP2b covered initially RCP2.6 and RCP6.0, a low emission and an intermediate stabilization scenario, with the high emission RCP8.5 scenario added at a later stage, leading to a lower hazard simulation availability (see table S2 for the scenarios covered by each impact model). The four GCMs were selected by availability of variables necessary for impact modeling and their position in the distribution of equilibrium climate sensitivity (ECS) in the CMIP5 ensemble. With an ECS of 4.1 °C for IPSL-CM5A-LR, 4.6 °C for HadGEM2-ES, 2.7 °C for MIROC5 and 2.4 °C for GFDL-ESM2M, the GCM selection includes two models at the lower and two at the upper end of the CMIP5 ensemble range (2.1 °C to 4.7 °C). The climate model data is regridded from its original resolution to the ISIMIP impact model grid at a spatial resolution of $0.5^\circ \times 0.5^\circ$. The climate model data is bias-adjusted (*16, 46*) to better represent the statistical distribution of observational weather data while preserving simulated trends. In addition, we use sub-daily output of the GCMs listed above that is not bias adjusted to force the high-resolution tropical-cyclone model.

Supplementary Text 6 – Wildfire simulations

The global burned area has seen a decrease in recent years, with the decrease explained mostly by a decrease in the number of fires associated with agricultural expansion (*108, 109*). In this

study, the wildfire simulations are designed to quantify the pure climate change effect on wildfire activity. To this end, we compute the change in burned area purely from a change in climate implemented via the GCM forcing, while keeping cropland area, population levels and other socioeconomic factors constant at 2005 levels. The vegetation models used here are suited for this type of analyses since their fire modules generally do not include human ignition (except for ORCHIDEE in which ignition depends on population density, with population density kept constant after 2005 in our simulation design). In addition, a historical land use-induced negative trend in burned area does not preclude that exposure to wildfire activity may rise in the next decades. Regional increases in wildfire activity have already been attributed to anthropogenic climate change (*98*) and fire weather is projected to substantially intensify in the coming decades (*110*). Moreover, exposure to fire may increase due to population expansion in fire-prone regions, an effect which may even outweigh changes in burned area (*111*). We account for this effect thanks to the use of annual gridded population density projections when spatially averaging the hazard maps. Combining our simulated climate-induced burned area changes with projected population density data suggest a clear increase wildfire exposure despite substantial uncertainties, corroborating a recent IPCC assessment of rising wildfire damage risk under continued global warming (*81, 82*).

Supplementary Figures

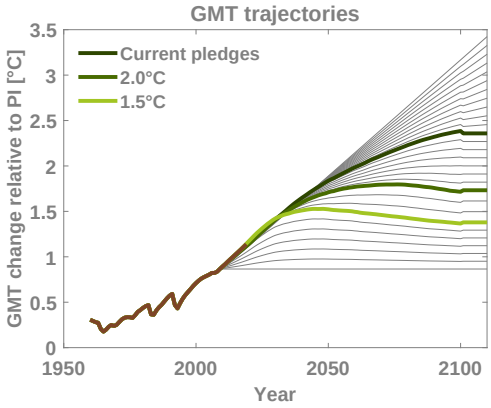

Supplementary Figure 1 | Global mean temperature pathways. Historical and future evolution of global mean temperature (GMT) anomalies relative to the pre-industrial (PI) reference scenario, taken here as the 1850–1900 average. Shown are three marker scenarios taken from the IPCC Special Report on Global Warming of 1.5°C (*54*), and 25 additional stylised pathways used for constructing fig. 2 (see Methods).

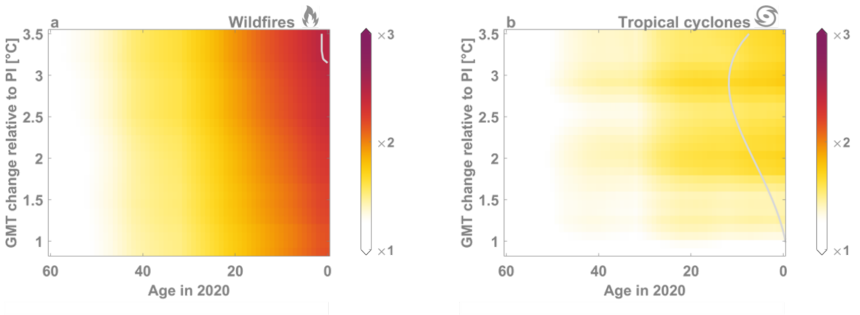

Supplementary Figure 2 | Lifetime wildfire and tropical cyclone exposure on the rise. Same as fig. 2, but for the extreme event categories **(a)** wildfires and **(b)** tropical cyclones.

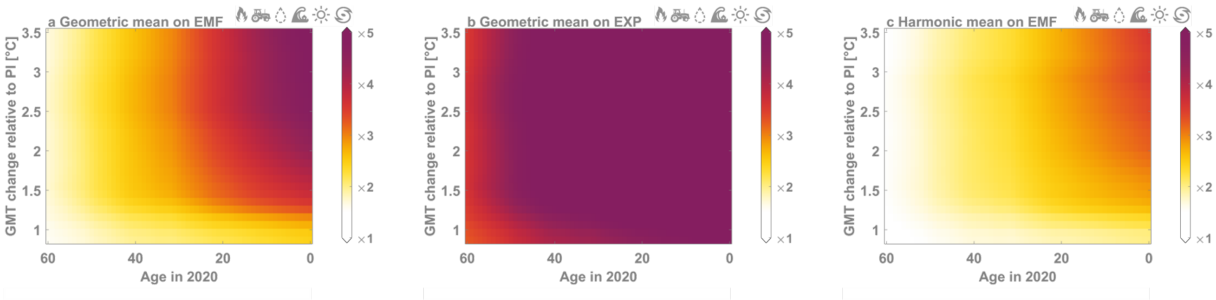

Supplementary Figure 3 | Cross-category lifetime exposure and influence of aggregation method on exposure sensitivity. (a) Same as fig. 2, but with exposure aggregated by computing the geometric mean across the exposure multiplication factor (EMF) per category, **(b)** Same as fig. 2, but with exposure aggregated by computing the geometric mean across the lifetime exposure (EXP), **(c)** Same as fig. 2, but with exposure aggregated by computing the harmonic mean across the EMF per category. We note that the second aggregation method (geometric mean on exposure) yields higher EMF values because the absence of events in one extreme event category results in zero cross-category exposure in a given country. As this occurs more frequently under pre-industrial control conditions, this leads to unrealistically low global-average pre-industrial control exposure values and hence artificially high EMF values.

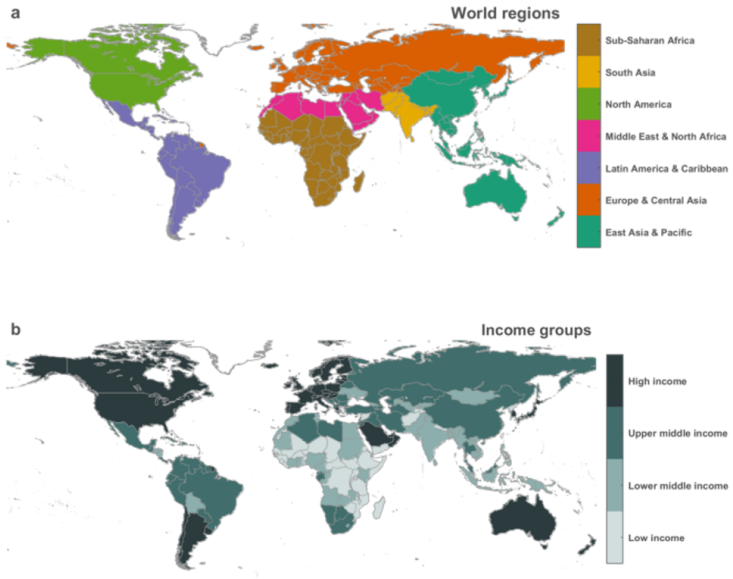

Supplementary Figure 4 | World Regions. Groups of countries based on **(a)** geographical location and **(b)** income category for which life expectancy data is available (*52*). The income groups are defined based on present-day conditions. The region definitions are taken from the World Bank (*112*) and abbreviated as follows (see e.g. fig. S11-12): East Asia & Pacific (EASP), Europe & Central Asia (EUCA), Latin America & Caribbean (LAMC), Middle East & North Africa (MENA), North America (NAM), South Asia (SAS), Sub-Saharan Africa (SSA).

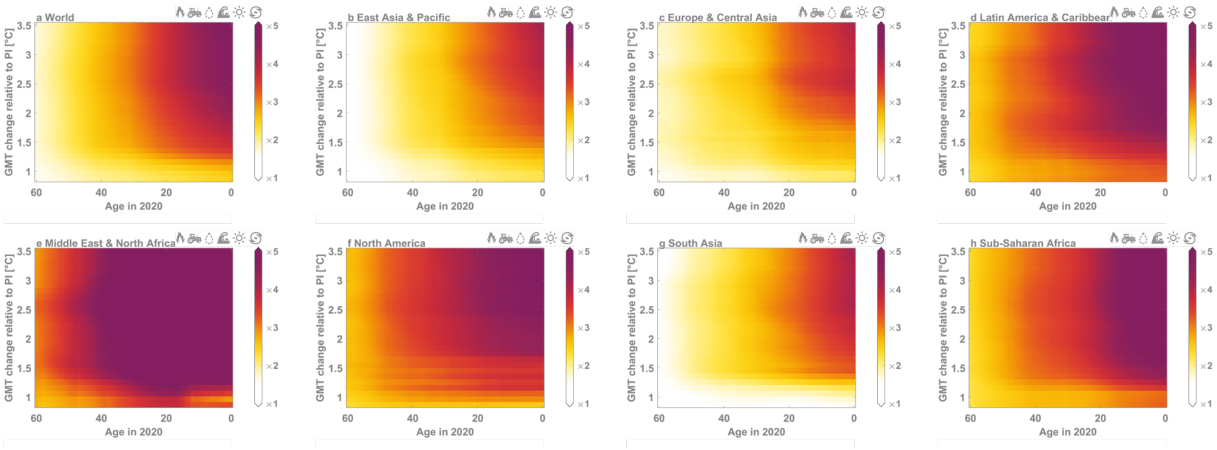

Supplementary Figure 5 | Regional lifetime exposure. Same as fig. S3a, but for world regions shown in fig. S4a.

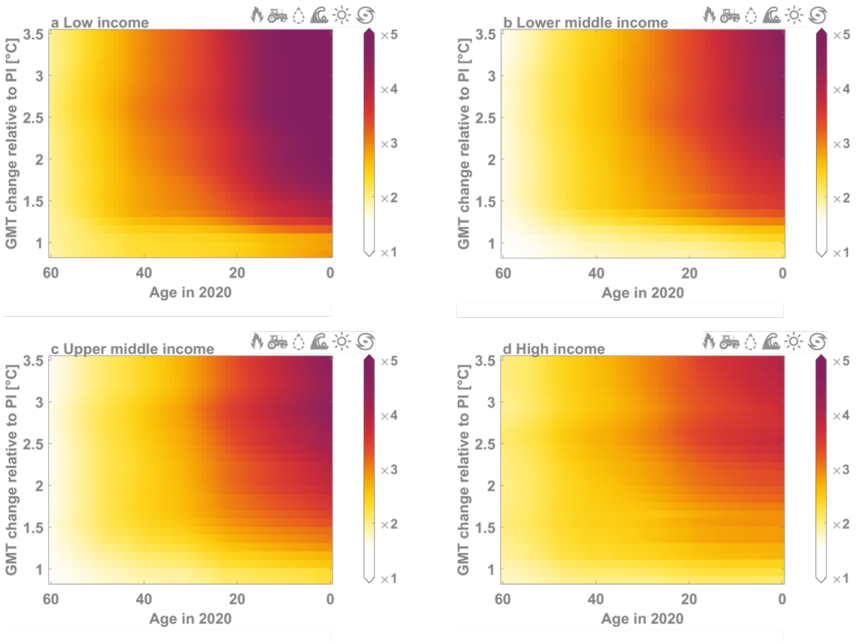

Supplementary Figure 6 | Income-based lifetime exposure. Same as fig. S3a, but for income group regions shown in fig. S4b.

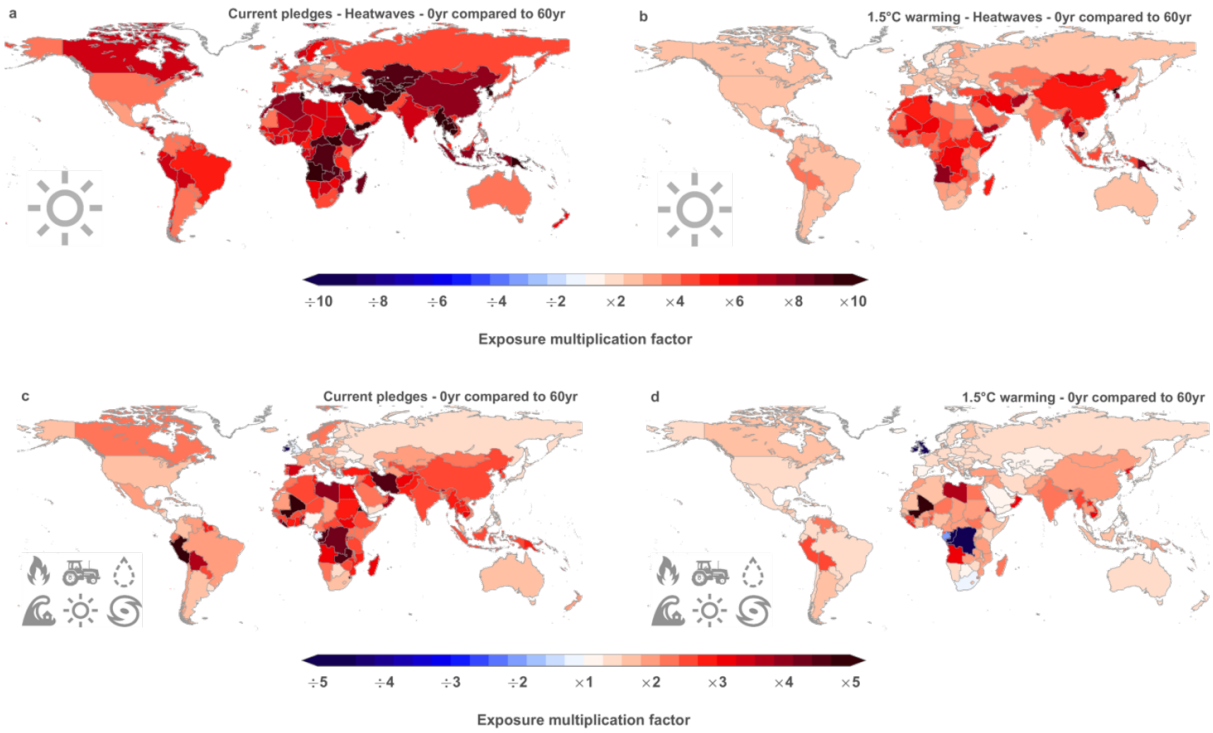

Supplementary Figure 7 | Local value of global mitigation. (**a,b**) Heatwave and (**c,d**) all-category exposure multiplication factors at the country scale for the 2020 birth cohort relative to the 1960 birth cohort under (**a,c**) the current pledges scenario and (**b,d**) the 1.5 °C scenario. Country-scale exposure multiplication factors aggregate within-country variability in population density and land fraction affected by extreme events.

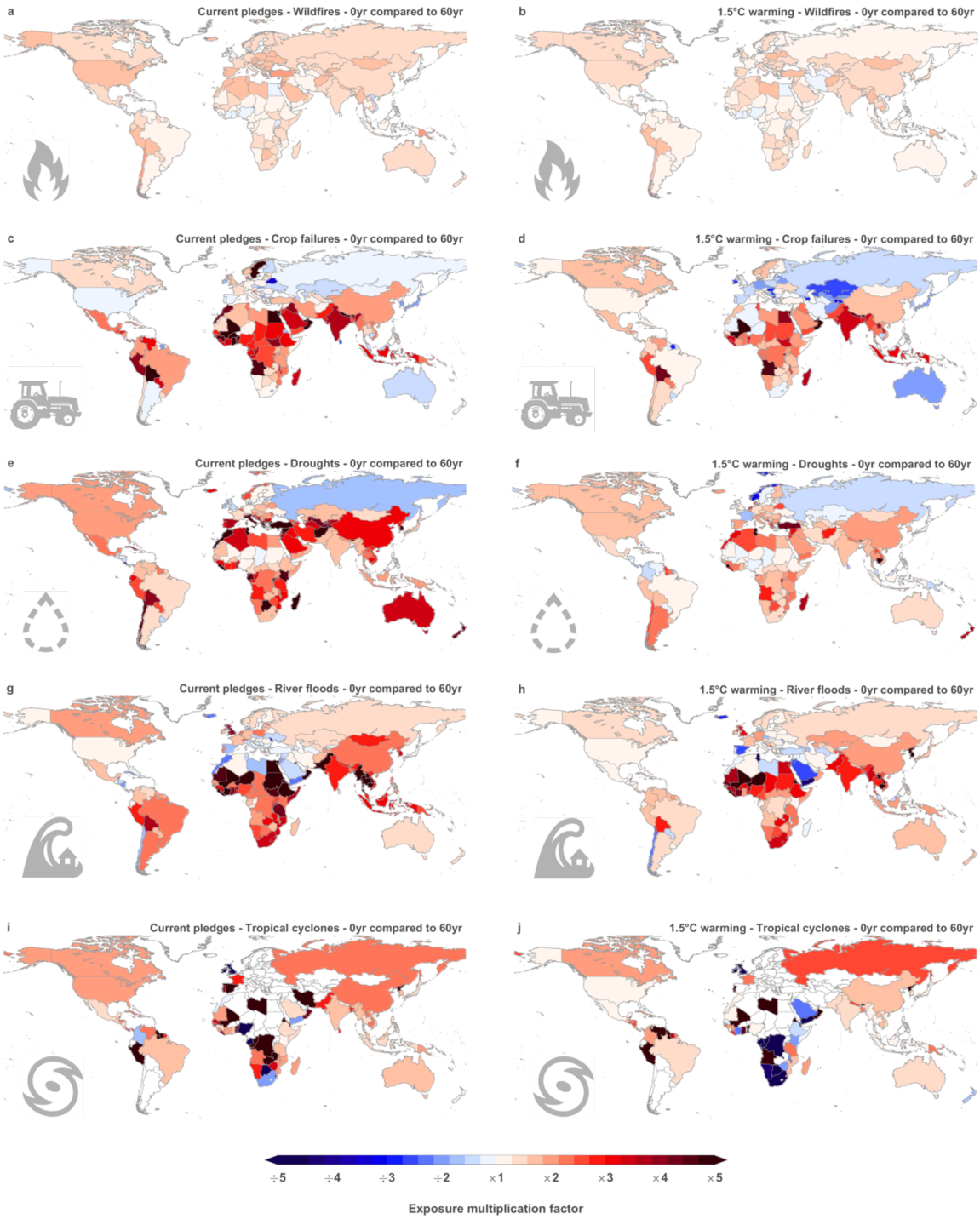

Supplementary Figure 8 | Country-scale exposure multiplication factors. Same as fig. S7, but for the extreme event categories **(a,b)** wildfires, **(c,d)** crop failures, **(e,f)** droughts, **(g,h)** river floods, and **(i,j)** tropical cyclones. Country-scale exposure multiplication factors aggregate within-country variability in population density and land fraction affected by extreme events. Note that the large tropical cyclone multiplication factors for some world regions with no or very low numbers of observed tropical cyclone landfalls (e.g. West and Southwest Africa, Western South America, Western Europe) are based on a small number of simulated tropical cyclones and should therefore be treated with caution.

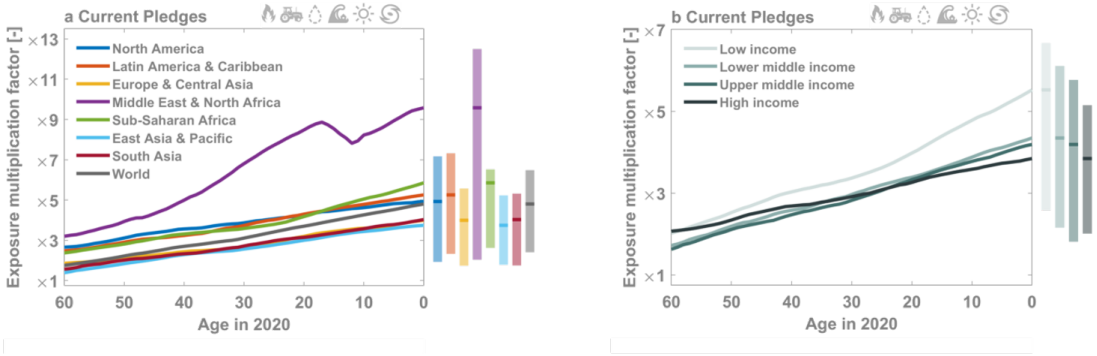

Supplementary Figure 9 | Uneven distribution of lifetime exposure. All-category exposure multiplication factors across birth cohorts under the current pledges scenario for a range of (**a**) geographic regions and (**b**) income groups (see fig. S4 for the region definitions (*112*)). The factors are computed relative to the mean exposure of a reference person with year-1960 life expectancy under pre-industrial climate conditions. The kink in the curve for the Middle East and North Africa for cohorts below 20 years in 2020 can be explained by the sudden drop in life expectancy for these cohorts in Iraq and Syria.

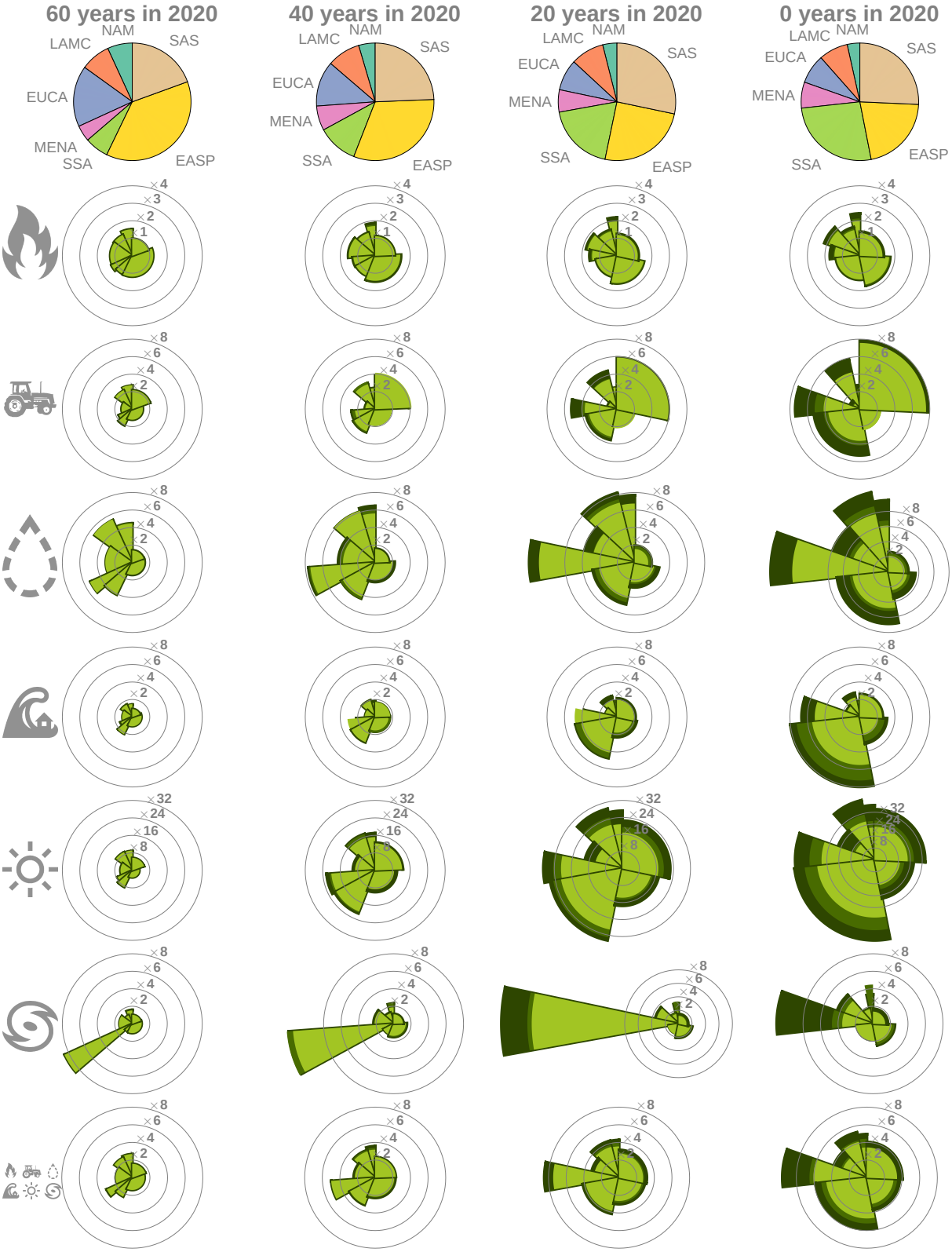

Supplementary Figure 10 | Exposure increase across world regions. Regional EMFs relative to the hypothetical pre-industrial reference cohort under 1.5 °C, 2.0 °C, and current pledges pathways (colored radial distance) per world region for all extreme event categories (rows) and cohorts 60, 40, 20, and 0 years old in 2020 (columns). The upper row and angle show the relative cohort size per region. Note the different radial scale for wildfires and heatwaves.

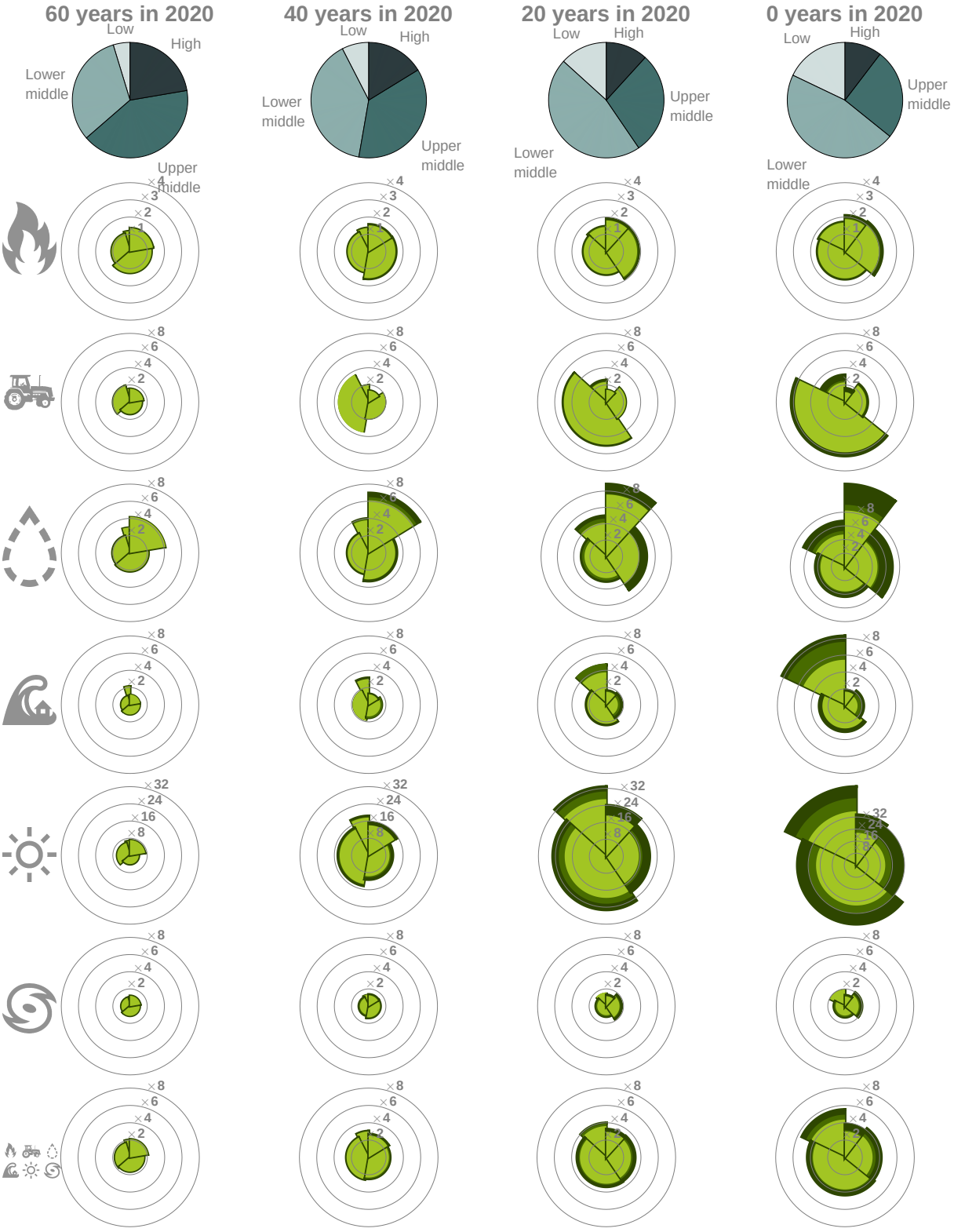

Supplementary Figure 11 | Exposure increase across income country groups. Same as fig. S10 but for income country groups defined in fig. S4b. Note the different radial scale for wildfires and heatwaves.

Supplementary Figure 12 | Exposure increase relative to the 1960 birth cohort across income country groups. Same as fig. S10 but using the 1960 birth cohort as reference for the EMF calculation. Note the different radial scale for heatwaves.

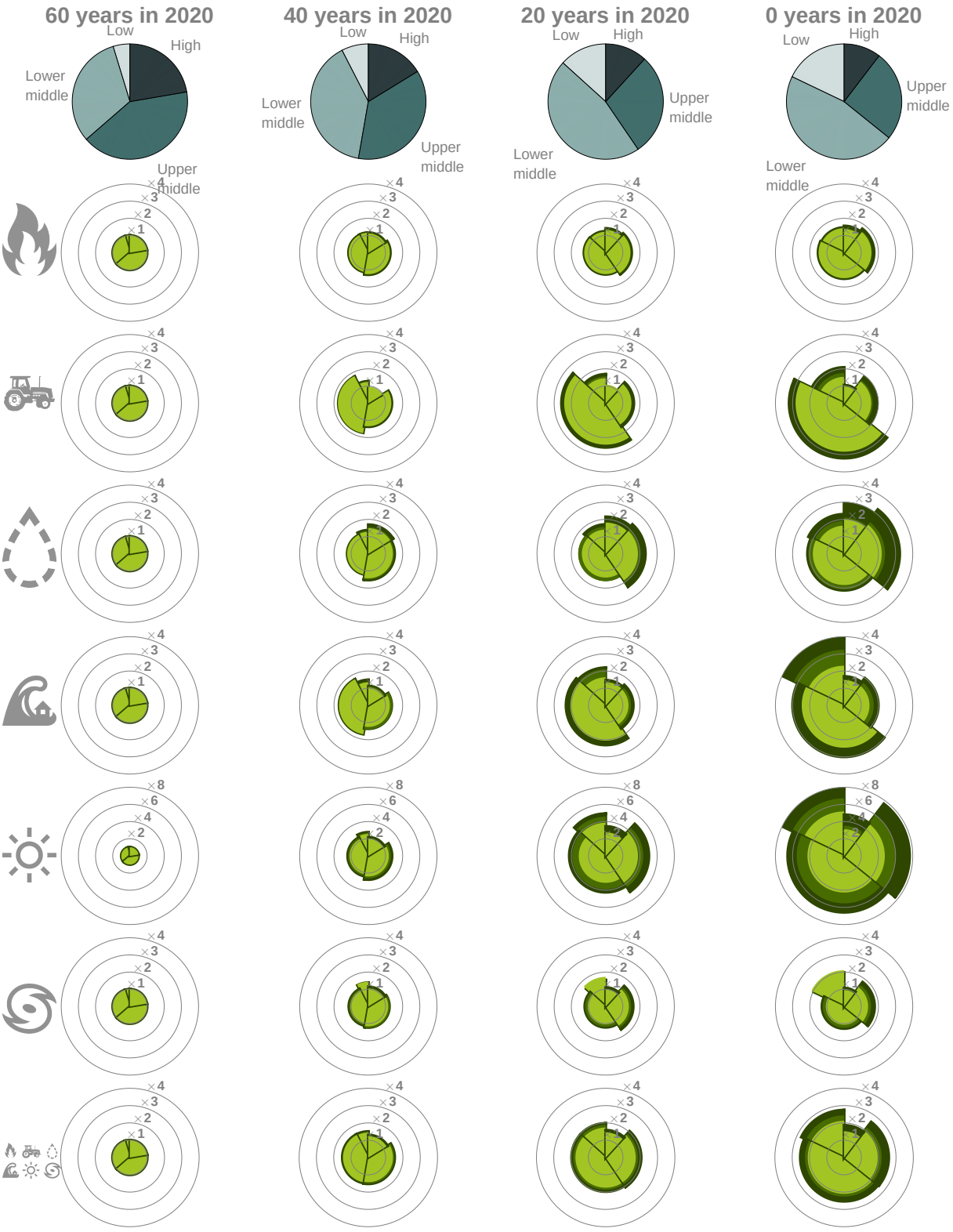

Supplementary Figure 13 | Exposure increase relative to the 1960 birth cohort across income country groups. Same as fig. S11 but using the 1960 birth cohort as reference for the EMF calculation. Note the different radial scale for heatwaves.

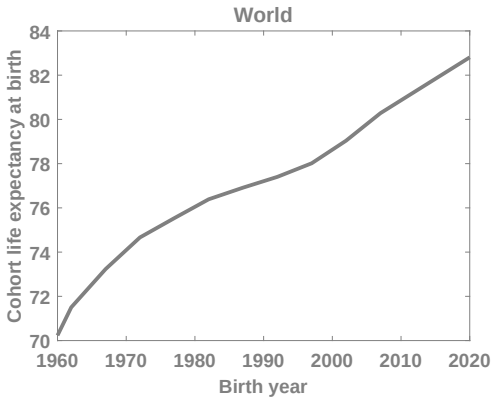

Supplementary Figure 14 | Life expectancy on the rise. Assumed increase in global cohort life expectancy at birth (adjusted for child mortality 0-4 -– see methods section).

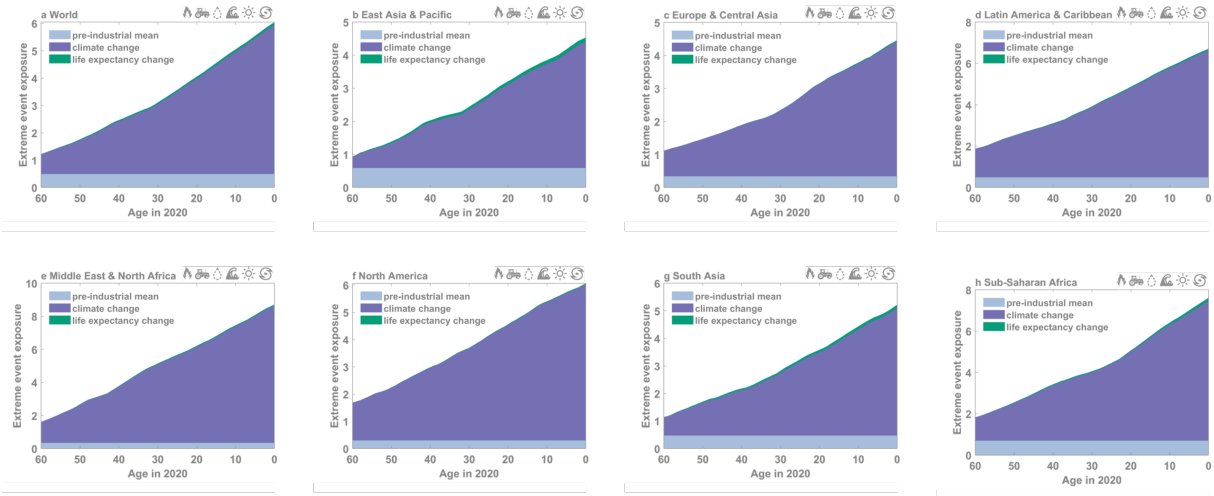

Supplementary Figure 15 | Drivers of increasing exposure across world regions. All-category exposure multiplication factors across birth cohorts separated by driver under the current pledges scenario for a range of geographic regions (see fig. S4a for the region definitions (*112*)). As the figure is based on exposure instead of EMF, we use the arithmetic mean instead of the geometric mean to aggregate the information across the categories.

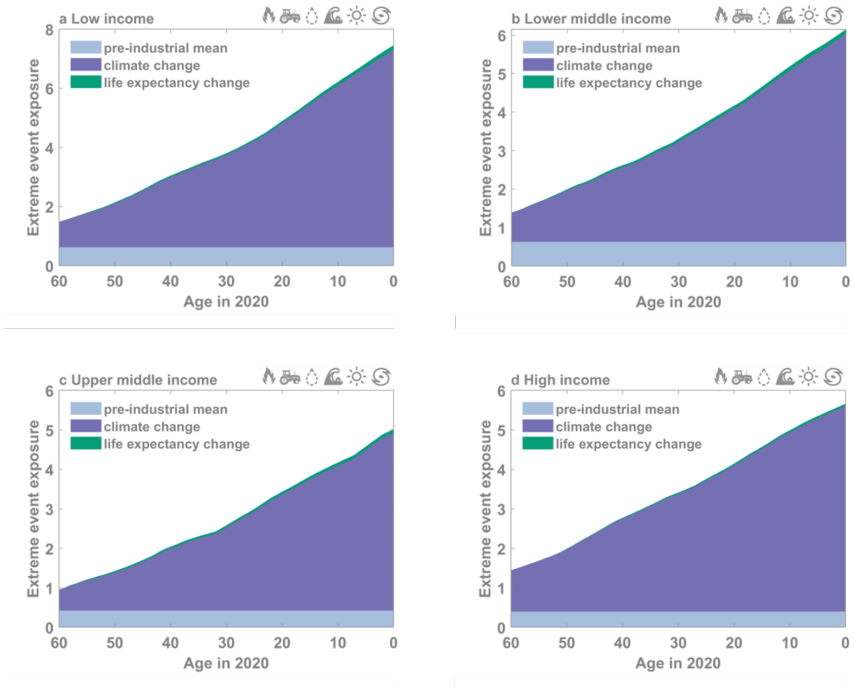

Supplementary Figure 16 | Drivers of increasing exposure across income country groups. Same as fig. S15, but for income country groups defined in fig. S4b. As the figure is based on exposure instead of EMF, we use the arithmetic mean instead of the geometric mean to aggregate the information across the categories.

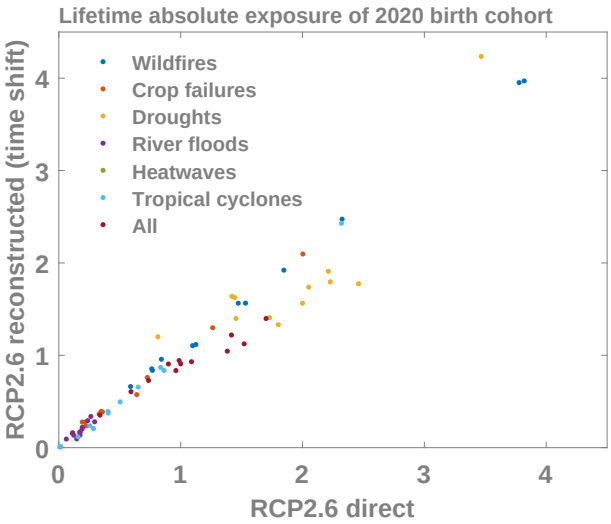

Supplementary Figure 17 | Evaluation of the time-shift approach. Lifetime extreme event exposure of the 2020 birth cohort under RCP2.6 computed using the original RCP2.6 simulations (x-axis) and by applying the time-shift approach to the RCP2.6, 6.0, and 8.5 simulations (y-axis). Each color represents an extreme event category and each dot represents the ensemble mean for one of the 12 considered regions (geographic regions, income categories, and global as defined in fig. S4).

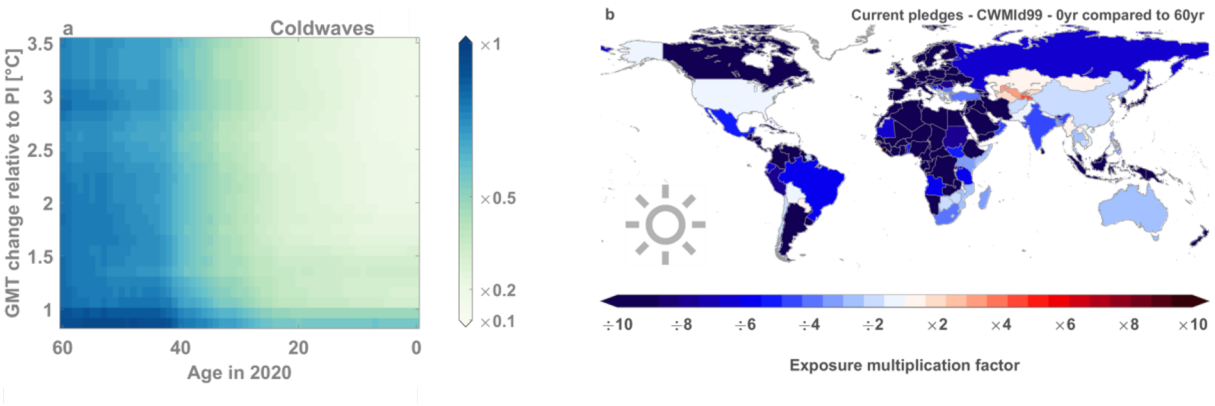

Supplementary Figure 18 | Cold spell exposure change. **(a)** Exposure multiplication factors across birth cohorts (x-axis) under a range of global warming trajectories (fig. S1) reaching 0.87 °C to 3.5 °C global mean temperature (GMT) anomalies in 2100 relative to the pre-industrial (PI) reference period (1850–1900; y-axis) for coldwaves. All factors are computed relative to the mean exposure of a hypothetical reference person living under pre-industrial climate conditions with year-1960 life expectancy. **(b)** Same as fig. S7a, but for CWMId.

Supplementary Tables

Supplementary Table 1 | Definition of extreme events. For each category, the number of impact models (M.) and future projections (P.) is reported. Further details are provided in the Methods section and in (*37*)

Event	M.	P.	Definition of land area exposed
Wildfire	5	53	Annual aggregate of monthly burned land area simulated by global vegetation models
Crop failure	3	24	Fraction of grid cell where one of the considered crops (maize, wheat, soy or rice) is grown and the corresponding crop yield falls short of the 2.5^{th} percentile of the pre-industrial reference distribution; crop-specific land area fractions are added up.
Drought	8	86	Entire grid cell if monthly soil moisture falls short of the 2.5^{th} percentile of the preindustrial reference distribution for at least 7 consecutive months.
River Flood	8	86	Flooding is assumed to occur whenever daily discharge ($0.5^\circ \times 0.5^\circ$ resolution) exceeds the preindustrial 100-year return level (i.e. the 99^{th} percentile); to derive the associated land area affected per grid cell, simulated runoff is translated into inundation areas (2.5' $\times$ 2.5' resolution) by CaMa-Flood (*68*).
Heatwave	1	12	Entire grid cell if the Heat Wave Magnitude Index daily (HWMId) (*70, 71*) of that year exceeds the 99^{th} percentile of the HWMId distribution under pre-industrial climate conditions of that grid cell. The HWMId is defined as the maximum magnitude of all hot periods occurring in a year, where a hot period is a period of at least 3 consecutive days with daily maximum temperature exceeding a threshold value T_{pi90} which is defined as the 90^{th} percentile of daily maximum temperatures under pre-industrial climate conditions, centered on a 31-day window. The magnitude of each hot period in a year is the sum of the daily magnitudes on the consecutive days composing the hot period, with daily magnitude calculated according to $M_d(T_d) = 0$ if $T_d \leq T_{\text{pi25}}$ else $(T_d - T_{\text{pi25}})/(T_{\text{pi75}} - T_{\text{pi25}})$, where T_d is the daily maximum temperature on day d of the hot period and T_{pi25} and T_{pi75} are the 25^{th} and 75^{th} percentile, respectively, of the annual maximum of the daily maximum temperature under pre-industrial climate conditions. To estimate T_{pi90}, T_{pi25}, and T_{pi75}, we use more than 400 years of daily maximum temperature data at $0.5^\circ \times 0.5^\circ$ spatial resolution representing pre-industrial climate conditions as available from the ISIMIP2b climate input data set. Based on these >400 years of temperature data we subsequently derive the 99^{th} percentile of the HWMId distribution under pre-industrial climate conditions.
Tropical cyclone	1	12	Fraction of grid cell exposed to 1-minute sustained hurricane-force winds ($\geq$64 kt) at least once a year ($0.1^\circ \times 0.1^\circ$ resolution); information required about wind fields is derived from center location and minimum pressure/maximum wind speed (*113, 114*).

Supplementary Table 2 | ISIMIP2b model simulations used for the analysis. Each model simulation consists of a concatenated historical and future (RCP2.6, 6.0 or 8.5) simulation done with one impact model (IM) and one global climate model (GCM). The last column indicates the number of simulation years available from the pre-industrial control simulation (PIcontrol). For tropical cyclones, each simulation represents the average of a 100-member ensemble of tropical cyclone tracks downscaled from GCM output (*38*).

Extreme	**IM**	**GCM**	**RCP**	**PIcontrol (years)**
Wildfires	CARAIB	GFDL-ESM2M	2.6, 6.0	439
Wildfires	CARAIB	HadGEM2-ES	2.6, 6.0	639
Wildfires	CARAIB	IPSL-CM5A-LR	2.6, 6.0	639
Wildfires	CARAIB	MIROC5	2.6, 6.0	639
Wildfires	LPJ-GUESS	GFDL-ESM2M	2.6, 6.0, 8.5	439
Wildfires	LPJ-GUESS	HadGEM2-ES	2.6, 6.0, 8.5	639
Wildfires	LPJ-GUESS	IPSL-CM5A-LR	2.6, 6.0, 8.5	639
Wildfires	LPJ-GUESS	MIROC5	2.6, 6.0, 8.5	639
Wildfires	LPJmL	GFDL-ESM2M	2.6, 6.0, 8.5	439
Wildfires	LPJmL	HadGEM2-ES	2.6, 6.0, 8.5	639
Wildfires	LPJmL	IPSL-CM5A-LR	2.6, 6.0, 8.5	639
Wildfires	LPJmL	MIROC5	2.6, 6.0, 8.5	639
Wildfires	ORCHIDEE	GFDL-ESM2M	2.6, 6.0, 8.5	239
Wildfires	ORCHIDEE	HadGEM2-ES	2.6, 6.0, 8.5	239
Wildfires	ORCHIDEE	IPSL-CM5A-LR	2.6, 6.0, 8.5	439
Wildfires	ORCHIDEE	MIROC5	2.6, 6.0, 8.5	239
Wildfires	VISIT	GFDL-ESM2M	2.6, 6.0, 8.5	439
Wildfires	VISIT	IPSL-CM5A-LR	2.6, 6.0, 8.5	639
Wildfires	VISIT	MIROC5	2.6, 6.0, 8.5	639
Crop failures	GEPIC	GFDL-ESM2M	2.6, 6.0	439
Crop failures	GEPIC	HadGEM2-ES	2.6, 6.0	639
Crop failures	GEPIC	IPSL-CM5A-LR	2.6, 6.0	639
Crop failures	GEPIC	MIROC5	2.6, 6.0	639
Crop failures	LPJmL	GFDL-ESM2M	2.6, 6.0	439
Crop failures	LPJmL	HadGEM2-ES	2.6, 6.0	639
Crop failures	LPJmL	IPSL-CM5A-LR	2.6, 6.0	639
Crop failures	LPJmL	MIROC5	2.6, 6.0	639
Crop failures	PEPIC	GFDL-ESM2M	2.6, 6.0	439
Crop failures	PEPIC	HadGEM2-ES	2.6, 6.0	639
Crop failures	PEPIC	IPSL-CM5A-LR	2.6, 6.0	639
Crop failures	PEPIC	MIROC5	2.6, 6.0	639
Droughts	CLM4.5	GFDL-ESM2M	2.6, 6.0, 8.5	239

Table 2 continued from previous page

Extreme	IM	GCM	RCP	PIcontrol (years)
Droughts	CLM4.5	HadGEM2-ES	2.6, 6.0, 8.5	239
Droughts	CLM4.5	IPSL-CM5A-LR	2.6, 6.0, 8.5	239
Droughts	CLM4.5	MIROC5	2.6, 6.0, 8.5	239
Droughts	H08	GFDL-ESM2M	2.6, 6.0, 8.5	439
Droughts	H08	HadGEM2-ES	2.6, 6.0, 8.5	639
Droughts	H08	IPSL-CM5A-LR	2.6, 6.0, 8.5	639
Droughts	H08	MIROC5	2.6, 6.0, 8.5	639
Droughts	LPJmL	GFDL-ESM2M	2.6, 6.0, 8.5	439
Droughts	LPJmL	HadGEM2-ES	2.6, 6.0, 8.5	639
Droughts	LPJmL	IPSL-CM5A-LR	2.6, 6.0, 8.5	639
Droughts	LPJmL	MIROC5	2.6, 6.0, 8.5	639
Droughts	JULES-W1	GFDL-ESM2M	2.6, 6.0, 8.5	439
Droughts	JULES-W1	HadGEM2-ES	2.6, 6.0, 8.5	639
Droughts	JULES-W1	IPSL-CM5A-LR	2.6, 6.0, 8.5	639
Droughts	JULES-W1	MIROC5	2.6, 6.0, 8.5	639
Droughts	MPI-HM	GFDL-ESM2M	2.6, 6.0	439
Droughts	MPI-HM	IPSL-CM5A-LR	2.6, 6.0	639
Droughts	MPI-HM	MIROC5	2.6, 6.0	639
Droughts	ORCHIDEE	GFDL-ESM2M	2.6, 6.0, 8.5	439
Droughts	ORCHIDEE	HadGEM2-ES	2.6, 6.0, 8.5	439
Droughts	ORCHIDEE	IPSL-CM5A-LR	2.6, 6.0, 8.5	639
Droughts	ORCHIDEE	MIROC5	2.6, 6.0, 8.5	439
Droughts	PCR-GLOBWB	GFDL-ESM2M	2.6, 6.0	439
Droughts	PCR-GLOBWB	HadGEM2-ES	2.6, 6.0	639
Droughts	PCR-GLOBWB	IPSL-CM5A-LR	2.6, 6.0	639
Droughts	PCR-GLOBWB	MIROC5	2.6, 6.0	639
Droughts	WaterGAP2	GFDL-ESM2M	2.6, 6.0, 8.5	439
Droughts	WaterGAP2	HadGEM2-ES	2.6, 6.0, 8.5	639
Droughts	WaterGAP2	IPSL-CM5A-LR	2.6, 6.0, 8.5	639
Droughts	WaterGAP2	MIROC5	2.6, 6.0, 8.5	639
River floods	CLM4.5	GFDL-ESM2M	2.6, 6.0, 8.5	439
River floods	CLM4.5	HadGEM2-ES	2.6, 6.0, 8.5	439
River floods	CLM4.5	IPSL-CM5A-LR	2.6, 6.0, 8.5	439
River floods	CLM4.5	MIROC5	2.6, 6.0, 8.5	439
River floods	H08	GFDL-ESM2M	2.6, 6.0, 8.5	439
River floods	H08	HadGEM2-ES	2.6, 6.0, 8.5	639
River floods	H08	IPSL-CM5A-LR	2.6, 6.0, 8.5	639
River floods	H08	MIROC5	2.6, 6.0, 8.5	639

Table 2 continued from previous page

Extreme	IM	GCM	RCP	PIcontrol (years)
River floods	LPJmL	GFDL-ESM2M	2.6, 6.0, 8.5	439
River floods	LPJmL	HadGEM2-ES	2.6, 6.0, 8.5	639
River floods	LPJmL	IPSL-CM5A-LR	2.6, 6.0, 8.5	639
River floods	LPJmL	MIROC5	2.6, 6.0, 8.5	639
River floods	JULES-W1	GFDL-ESM2M	2.6, 6.0, 8.5	439
River floods	JULES-W1	HadGEM2-ES	2.6, 6.0, 8.5	439
River floods	JULES-W1	IPSL-CM5A-LR	2.6, 6.0, 8.5	639
River floods	JULES-W1	MIROC5	2.6, 6.0, 8.5	439
River floods	MPI-HM	GFDL-ESM2M	2.6, 6.0	439
River floods	MPI-HM	IPSL-CM5A-LR	2.6, 6.0	639
River floods	MPI-HM	MIROC5	2.6, 6.0	639
River floods	ORCHIDEE	GFDL-ESM2M	2.6, 6.0, 8.5	439
River floods	ORCHIDEE	HadGEM2-ES	2.6, 6.0, 8.5	439
River floods	ORCHIDEE	IPSL-CM5A-LR	2.6, 6.0, 8.5	639
River floods	ORCHIDEE	MIROC5	2.6, 6.0, 8.5	439
River floods	PCR-GLOBWB	GFDL-ESM2M	2.6, 6.0	439
River floods	PCR-GLOBWB	HadGEM2-ES	2.6, 6.0	639
River floods	PCR-GLOBWB	IPSL-CM5A-LR	2.6, 6.0	639
River floods	PCR-GLOBWB	MIROC5	2.6, 6.0	639
River floods	WaterGAP2	GFDL-ESM2M	2.6, 6.0, 8.5	439
River floods	WaterGAP2	HadGEM2-ES	2.6, 6.0, 8.5	639
River floods	WaterGAP2	IPSL-CM5A-LR	2.6, 6.0, 8.5	639
River floods	WaterGAP2	MIROC5	2.6, 6.0, 8.5	639
Heatwaves	HWMId-humidex	GFDL-ESM2M	2.6, 6.0, 8.5	439
Heatwaves	HWMId-humidex	HadGEM2-ES	2.6, 6.0, 8.5	639
Heatwaves	HWMId-humidex	IPSL-CM5A-LR	2.6, 6.0, 8.5	639
Heatwaves	HWMId-humidex	MIROC5	2.6, 6.0, 8.5	639
Tropical cyclones	KE-TG-meanfield	GFDL-ESM2M	2.6, 6.0, 8.5	439
Tropical cyclones	KE-TG-meanfield	HadGEM2-ES	2.6, 6.0, 8.5	439
Tropical cyclones	KE-TG-meanfield	IPSL-CM5A-LR	2.6, 6.0, 8.5	639
Tropical cyclones	KE-TG-meanfield	MIROC5	2.6, 6.0, 8.5	639

Supplementary References

16. K. Frieler, *et al.*, *Geoscientific Model Development* **10**, 4321 (2017).

17. M. Dury, *et al.*, *iForest - Biogeosciences and Forestry* **4**, 82 (2011).

18. B. Smith, *et al.*, *Biogeosciences* **11**, 2027 (2014).

19. S. Schaphoff, *et al.*, *Geoscientific Model Development* **11**, 1343 (2018).

20. S. Schaphoff, *et al.*, *Geoscientific Model Development* **11**, 1377 (2018).

21. M. Guimberteau, *et al.*, *Geoscientific Model Development* **11**, 121 (2018).

22. A. Ito, T. Oikawa, *Ecological Modelling* **151**, 143 (2002).

23. A. Ito, M. Inatomi, *Journal of Hydrometeorology* **13**, 681 (2012).

24. C. Folberth, T. Gaiser, K. C. Abbaspour, R. Schulin, H. Yang, *Agriculture, Ecosystems Environment* **151**, 21 (2012).

25. W. Liu, *et al.*, *Agricultural and Forest Meteorology* **221**, 164 (2016).

26. W. Liu, *et al.*, *Science of The Total Environment* **572**, 526 (2016).

27. D. M. Lawrence, *et al.*, *Journal of Advances in Modeling Earth Systems* **3**, M03001 (2011).

28. W. Thiery, *et al.*, *Journal of Geophysical Research: Atmospheres* **122**, 1403 (2017).

29. N. Hanasaki, S. Yoshikawa, Y. Pokhrel, S. Kanae, *Hydrology and Earth System Sciences* **22**, 789 (2018).

30. M. J. Best, *et al.*, *Geoscientific Model Development* **4**, 677 (2011).

31. S. Hagemann, L. D. Gates, *Climate Dynamics* **21**, 349 (2003).

32. T. Stacke, S. Hagemann, *Hydrology and Earth System Sciences* **16**, 2915 (2012).

33. Y. Wada, D. Wisser, M. F. P. Bierkens, *Earth System Dynamics* **5**, 15 (2014).

34. Y. Wada, I. E. M. de Graaf, L. P. H. van Beek, *Journal of Advances in Modeling Earth Systems* **8**, 735 (2016).

35. H. Müller Schmied, *et al.*, *Hydrology and Earth System Sciences* **18**, 3511 (2014).

36. H. Müller Schmied, *et al.*, *Hydrology and Earth System Sciences* **20**, 2877 (2016).

37. S. Lange, *et al.*, *Earth's Future* **8**, 1 (2020).

38. K. A. Emanuel, *Proceedings of the National Academy of Sciences* **110**, 12219 (2013).

39. Y. Pokhrel, *et al.*, *Nature Climate Change* **11**, 226 (2021).

40. L. Gudmundsson, *et al.*, *Science* **371**, 1159 (2021).

41. R. Reinecke, *et al.*, *Hydrology and Earth System Sciences* **25**, 787 (2021).

42. C.-E. Telteu, *et al.*, *Geoscientific Model Development* **14**, 3843 (2021).

43. I. Vanderkelen, *et al.*, *Geophysical Research Letters* **47** (2020).

44. A. Ito, *et al.*, *Environmental Research Letters* **15**, 044006 (2020).

45. R. Wartenburger, *et al.*, *Environmental Research Letters* **13**, 075001 (2018).

46. S. Lange, *Earth System Dynamics* **9**, 627 (2018).

47. J. P. Dunne, *et al.*, *Journal of Climate* **25**, 6646 (2012).

48. C. D. Jones, *et al.*, *Geoscientific Model Development* **4**, 543 (2011).

49. J.-L. Dufresne, *et al.*, *Climate Dynamics* **40**, 2123 (2013).

50. M. Watanabe, *et al.*, *Journal of Climate* **23**, 6312 (2010).

51. K. E. Taylor, R. J. Stouffer, G. A. Meehl, *Bulletin of the American Meteorological Society* **93**, 485 (2012).

52. United Nations Department of Economic and Social Affairs Population Division, World Population Prospects 2019 (2019).

53. J. R. Goldstein, K. W. Wachter, *Population Studies* **60**, 257 (2006).

54. J. Rogelj, *et al.*, *Mitigation Pathways Compatible with 1.5C in the Context of Sustainable Development. In: Global Warming of 1.5C. An IPCC Special Report on the impacts of global warming of 1.5C above pre-industrial levels and related global greenhouse gas emission pathw*, V. Masson-Delmotte, *et al.*, eds. (2018), pp. 93–174.

55. J. Rogelj, *et al.*, *Nature Climate Change* **8**, 325 (2018).

56. D. Huppmann, J. Rogelj, E. Kriegler, V. Krey, K. Riahi, *Nature Climate Change* **8**, 1027 (2018).

57. D. Huppmann, *et al.*, IAMC 1.5C Scenario Explorer and Data hosted by Integrated Assessment Modeling Consortium International Institute for Applied Systems Analysis (2019).

58. A. Grubler, *et al.*, *Nature Energy* **3**, 515 (2018).

59. V. Krey, *et al.*, *MESSAGE-GLOBIOM 1.0 Documentation* (International Institute for Applied Systems Analysis (IIASA), 2016).

60. E. Stehfest, *et al.*, *Integrated Assessment of Global Environmental Change with IMAGE 3.0: Model description and policy applications* (PBL Netherlands Environmental Assessment Agency, The Hague, 2014).

61. K. K. Goldewijk, A. Beusen, J. Doelman, E. Stehfest, *Earth System Science Data* **9**, 927 (2017).

62. B. Jones, B. C. O'Neill, *Environmental Research Letters* **11**, 084003 (2016).

63. O. Fricko, *et al.*, *Global Environmental Change* **42**, 251 (2017).

64. S. KC, M. Potancokova, R. Bauer, A. Goujon, E. Striessnig, Summary of Data, Assumptions and Methods for New Wittgenstein Centre for Demography and Global Human Capital (WIC) Population Projections by Age, Sex and Level of Education for 195 Countries to 2100, *Tech. rep.*, International Institute for Applied Systems Analysis (2013).

65. W. Lutz, A. Goujon, S. KC, M. Stonawski, N. Stilianakis, *Demographic and human capital scenarios for the 21st century: 2018 assessment for 201 countries* (Publications Office of the European Union, 2018).

66. S. I. Seneviratne, *et al.*, *Managing the Risks of Extreme Events and Disasters to Advance Climate Change Adaptation*, C. Field, *et al.*, eds. (Cambridge University Press, Cambridge, UK, 2012), pp. 109–230.

67. F. Zhao, *et al.*, *Environmental Research Letters* **12**, 075003 (2017).

68. D. Yamazaki, S. Kanae, H. Kim, T. Oki, *Water Resources Research* **47**, 9726 (2011).

69. IPCC, *Climate Change 2013: The Physical Science Basis. Contribution of Working Group I to the Fifth Assessment Report of the Intergovernmental Panel on Climate Change* pp. 1447–1466 (2013).

70. S. Russo, J. Sillmann, E. M. Fischer, *Environmental Research Letters* **10**, 124003 (2015).

71. S. Russo, J. Sillmann, A. Sterl, *Scientific Reports* **7**, 7477 (2017).

72. N. Herger, B. M. Sanderson, R. Knutti, *Geophysical Research Letters* **42**, 3486 (2015).

73. R. James, R. Washington, C.-F. Schleussner, J. Rogelj, D. Conway, *WIREs Climate Change* **8**, e457 (2017).

74. M. Allen, *et al.*, *Global Warming of 1.5C. An IPCC Special Report on the impacts of global warming of 1.5C above pre-industrial levels and related global greenhouse gas emission pathways, in the context of strengthening the global response to the threat of climate change*, V. Masson-Delmotte, *et al.*, eds. (2018), pp. 49–91.

75. P. a. Stott, D. a. Stone, M. R. Allen, *Nature* **432**, 610 (2004).

76. E. M. Fischer, R. Knutti, *Nature Climate Change* **5**, 560 (2015).

77. W. Thiery, *et al.*, *Nature Communications* **11**, 290 (2020).

78. X. Zhang, G. Hegerl, F. W. Zwiers, J. Kenyon, *Journal of Climate* **18**, 1641 (2005).

79. S. Sippel, *et al.*, *Geophysical Research Letters* **42**, 9990 (2015).

80. IPCC, *Climate Change 2014: Impacts, Adaptation, and Vulnerability. Part A: Global and Sectoral Aspects. Contribution of Working Group II to the Fifth Assessment Report of the Intergovernmental Panel on Climate Change*, C. Field, *et al.*, eds. (2014), pp. 1–32.

81. M. Hurlbert, *et al.*, *Climate Change and Land: an IPCC special report on climate change, desertification, land degradation, sustainable land management, food security, and greenhouse gas fluxes in terrestrial ecosystems*, P. Shukla, *et al.*, eds. (IPCC, 2019), pp. 673–800.

82. Z. Zommers, *et al.*, *Nature Reviews Earth and Environment* **1**, 516 (2020).

83. M. Andrijevic, J. Crespo Cuaresma, T. Lissner, A. Thomas, C. F. Schleussner, *Nature Communications* **11**, 1 (2020).

84. J. Rogelj, *et al.*, *Nature* **534**, 631 (2016).

85. UNEP, Emissions Gap Report 2019, *Tech. rep.*, United Nations Environment Programme (2019).

86. W. Thiery, *et al.*, *Nature Communications* **7**, 12786 (2016).

87. N. Souverijns, W. Thiery, M. Demuzere, N. P. M. V. Lipzig, *Environmental Research Letters* **11**, 114011 (2016).

88. J. Zscheischler, *et al.*, *Nature Reviews Earth and Environment* **1**, 333 (2020).

89. S. E. Perkins-Kirkpatrick, S. C. Lewis, *Nature Communications* **11**, 3357 (2020).

90. F. Piontek, *et al.*, *Proceedings of the National Academy of Sciences* **111**, 3233 (2014).

91. J. Zscheischler, S. I. Seneviratne, *Science Advances* **3**, e1700263 (2017).

92. K. Kornhuber, *et al.*, *Nature Climate Change* **10**, 48 (2020).

93. C.-F. Schleussner, *et al.*, *Environmental Research Letters* **13**, 064007 (2018).

94. F. Gaupp, J. Hall, S. Hochrainer-Stigler, S. Dadson, *Nature Climate Change* **10**, 54 (2020).

95. A. J. Reed, *et al.*, *Proceedings of the National Academy of Sciences* **112**, 12610 (2015).

96. M. Mengel, A. Nauels, J. Rogelj, C.-F. Schleussner, *Nature Communications* **9**, 601 (2018).

97. A. Nauels, *et al.*, *Proceedings of the National Academy of Sciences* **116**, 23487 (2019).

98. J. T. Abatzoglou, A. P. Williams, *Proceedings of the National Academy of Sciences* (2016).

99. J. S. Pal, E. A. B. Eltahir, *Nature Climate Change* **6**, 197 (2016).

100. E.-S. Im, J. S. Pal, E. A. B. Eltahir, *Science Advances* **3**, e1603322 (2017).

101. F. Saeed, C. F. Schleussner, M. Ashfaq, *Geophysical Research Letters* **48** (2021).

102. O. Brousse, *et al.*, *International Journal of Climatology* **40**, 4586 (2020).

103. O. Brousse, *et al.*, *Environmental Research Letters* **15**, 124051 (2020).

104. L. H. Meyer, F. Schuppert, H. Stelzer, A. Placani, *Living with Uncertainty* (Cambridge University Press, Cambridge, 2009), pp. 72–117.

105. W. Nordhaus, *Science* **317**, 1682 (2007).

106. K. E. Taylor, R. J. Stouffer, G. A. Meehl, *Bulletin of the American Meteorological Society* **93**, 485 (2012).

107. M. Meinshausen, *et al.*, *Climatic Change* **109**, 213 (2011).

108. N. Andela, *et al.*, *Science* **356**, 1356 (2017).

109. V. K. Arora, J. R. Melton, *Nature Communications* **9**, 1326 (2018).

110. J. T. Abatzoglou, A. P. Williams, R. Barbero, *Geophysical Research Letters* **46**, 326 (2019).

111. W. Knorr, A. Arneth, L. Jiang, *Nature Climate Change* **6**, 781 (2016).

112. The World Bank, Life expectancy at birth (2020).

113. K. Emanuel, *Nature* **436**, 686 (2005).

114. T. Geiger, K. Frieler, D. N. Bresch, *Earth System Science Data* **10**, 185 (2018).